

Substrate effects on charged defects in two-dimensional materials

Dan Wang¹ and Ravishankar Sundararaman^{1,*}

¹*Department of Materials Science and Engineering, Rensselaer Polytechnic Institute, 110 8th Street, Troy, NY*

(Dated: August 15, 2019)

Two-dimensional (2D) materials are strongly affected by the dielectric environment including substrates, making it an important factor in designing materials for quantum and electronic technologies. Yet, first-principles evaluation of charged defect energetics in 2D materials typically do not include substrates due to the high computational cost. We present a general continuum model approach to incorporate substrate effects directly in density-functional theory calculations of charged defects in the 2D material alone. We show that this technique accurately predicts charge defect energies compared to much more expensive explicit substrate calculations, but with the computational expediency of calculating defects in free-standing 2D materials. Using this technique, we rapidly predict the substantial modification of charge transition levels of two defects in MoS₂ and ten defects promising for quantum technologies in hBN, due to SiO₂ and diamond substrates. This establishes a foundation for high-throughput computational screening of new quantum defects in 2D materials that critically accounts for substrate effects.

I. INTRODUCTION

Point defects such as vacancies and substitutional impurities play a central role in determining the optoelectronic properties of 2D materials desirable for electronic devices and quantum information applications.^{1–6} Their versatile functionality ranges from providing free carriers for charge transport in 2D semiconductors^{7–9} to encoding information in spin states for compact solid-state qubits.^{10–14} The complexity of controllably synthesizing, identifying and measuring properties of point defects necessitates first-principles computational predictions based on density-functional theory (DFT) to first screen for desirable defects and predict experimental signatures to aid their identification. In 2D materials, calculating energies of charged defects is complicated by the weak and highly anisotropic screening in these systems.¹⁵ The energy of a 2D supercell containing a charged defect diverges with cell size due to strong Coulomb interactions of the defect charge with its periodic images and compensating background.¹⁶ Several complementary approaches specialized for charged defects in 2D materials^{15–17} have made it possible to reliably predict charge transition levels and engineer defects in free-standing 2D materials.^{18–24}

However, 2D materials in most experiments and device configurations are not free-standing and are instead deposited, grown or transferred onto a substrate. The substrate is typically an integral part of developing and utilizing 2D materials, critical for nucleation during synthesis and mechanical stability in operation, and it is an unavoidable modification introduced to tune its properties. A thorough understanding of defect properties in 2D materials would therefore be unattainable without taking substrate effects into account. Yet, most computational studies of defects in 2D materials to date ignore substrates primarily due to the extremely high computational cost. Taking the example of monolayer MoS₂ on an SiO₂ substrate here, a typical 6×6 defect supercell calculation of a free-standing monolayer would require 108 atoms, but including a substrate with a minimal slab of

SiO₂(0001) with six atomic layers increases this to 428 atoms with a 60× increase in computational cost of plane-wave DFT calculations. Repeating such calculations for a large number of substitutional or interstitial impurities with different elements, vacancy configurations and complexes thereof in order to identify ideal defect candidates *on specific substrates* remains a formidable challenge.

One approach to eliminate this problem would be to remove the substrate atoms from the DFT calculations, and instead approximately capture their effect on the 2D material and defect. Electronic structure calculations in liquid and electrochemical environments have long had to deal with large numbers of *environment* atoms: practical approaches replace the liquid environment with the response of an appropriately determined dielectric cavity.^{25–27} Recent developments of such techniques have facilitated accurate first-principles calculations of complex chemical processes in electrochemical environments, with virtually insignificant computational expense beyond conventional DFT calculations in vacuum.^{28–34} Analogously, continuum models of substrates could enable rapid computational design of defects in realistic 2D material configurations that include substrates.

In this paper, we present a continuum model approach for capturing substrate effects in DFT calculations of the 2D material alone, which combined with charged defect correction schemes, provides an efficient and general method for evaluating charged defects in realistic 2D material configurations. We benchmark this methodology by predicting ionization energies of Re and Nb substitution defects (Re_{Mo} and Nb_{Mo}) in MoS₂ on substrate SiO₂ (MoS₂/SiO₂) and find the lowering of ionization energy due to increased screening from the substrate to be in excellent agreement with DFT calculations that explicitly include the substrate. We then use the so-proven method to predict the transition levels of ten promising defects in hBN on SiO₂ and diamond substrates (hBN/SiO₂ and hBN/Diamond), and show that these defect levels remain deep enough for applications in quantum technologies.

II. THEORY AND METHODS

A. Charge transition level and Ionization Energy

The formation energy of a defect with charge q is^{35,36}

$$E_f(q) = E_{\text{tot}}(q) - E_{\text{host}} + \sum_i N_i \mu_i + q \mu_e, \quad (1)$$

where $E_{\text{tot}}(q)$ and E_{host} are the total energies of the material with and without the defect, involving an exchange of N_i atoms of each species i with chemical potential μ_i . The electron chemical potential μ_e ranges from the valence band maximum ε_{VBM} to the conduction band minimum ε_{CBM} .

The calculation of $E_{\text{tot}}(q)$ involves a supercell with a net charge, which requires a scheme for correcting the diverging Coulomb interaction energy with periodic images. We employ the model-charge correction scheme described in detail in Refs. 17 and 18. Briefly, this technique corrects the energy and potential of the periodic DFT calculation by comparing Poisson equation solutions for a spherical Gaussian model of the defect charge interacting with a planar model for the anisotropic dielectric response of the material in periodic versus isolated boundary conditions. The anisotropic dielectric function of the 2D material is also calculated from first principles as described in Ref. 18. (See Supplemental Material for details.) We previously showed this technique to be the most robust for 2D materials, requiring no empirical parameters or cell-size extrapolation, and with all quantities extracted purely from DFT calculations of the material.¹⁸

Once we can calculate individual charged defect formation energies using this scheme, we can evaluate the charge transition level (CTL) of the defect, defined as the electron chemical potential μ_e at which two adjacent charge states q and q' have equal formation energy. Solving for μ_e from $E_f(q) = E_f(q')$ using (1) yields

$$\mu(q|q') = \frac{E_{\text{tot}}(q) - E_{\text{tot}}(q')}{q' - q}. \quad (2)$$

For donor defects which transition from $q = +1$ to $q = 0$, the transition level relative to the CBM is the donor ionization energy,

$$\text{IE}_d \equiv \varepsilon_{\text{CBM}} - \mu(+1|0) = E_{\text{tot}}(+1) - E_{\text{tot}}(0) + \varepsilon_{\text{CBM}}, \quad (3)$$

while for acceptor defects which transition from $q = 0$ to $q = -1$, the transition level relative to the VBM is the acceptor ionization energy,

$$\text{IE}_a \equiv \mu(0|-1) - \varepsilon_{\text{VBM}} = E_{\text{tot}}(-1) - E_{\text{tot}}(0) - \varepsilon_{\text{VBM}}. \quad (4)$$

Substrates strongly influence these ionization energies of defects in 2D materials, and we evaluate these in selected test cases by directly computing E_{tot} of a system containing the 2D material, defect and the substrate. However, such calculations are extremely expensive and we need a technique to account for substrate effects at reduced computational expense.

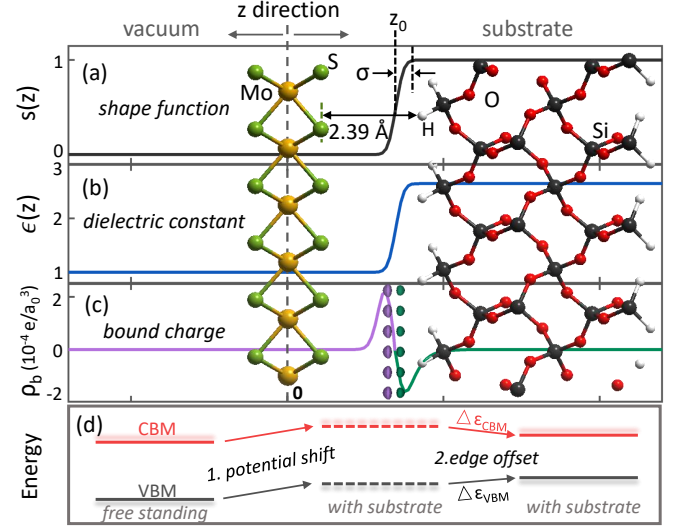


FIG. 1. Continuum model of SiO₂ substrate specified by (a) ‘shape function’ $s(z)$ switching from 0 outside substrate to 1 within, transitioning with width σ centered at location z_0 , relative to MoS₂ monolayer centered at $z = 0$. (b) Corresponding dielectric function and (c) bound charge induced in substrate. (d) Scheme for evaluating substrate effects on band edge positions, accounting for rigid shift due to the substrate potential from the continuum calculation and edge shifts ($\Delta \varepsilon_{\text{CBM}}$, $\Delta \varepsilon_{\text{VBM}}$) from an explicit calculation of the perfect 2D material on the substrate.

B. Continuum model for substrate effects

The challenge of accounting for a large number of atoms in an environment, analogous to the substrate in the present case, has been addressed extensively using continuum methods for capturing solvent effects in liquid-phase electronic structure calculations.^{25–27,32–34} While these continuum solvation techniques vary greatly in details, they share one common aspect: they capture the dominant electrostatic interaction of the environment by placing the ‘solute’ system in a dielectric cavity. The dielectric bound charge induced at the surface of this cavity then approximates the induced charges in the environment atoms, which are now removed from the electronic structure calculation. These models parametrize the cavity, often described in terms of a smooth cavity shape function $s(\mathbf{r})$ that goes from 0 in the solute region to 1 in the solvent (environment) region,³² and constrain parameters by fitting to solvation free energies determined from temperature-dependent solubility measurements.

We can similarly replace the dielectric effect of the substrate by replacing it with a dielectric slab described by a smooth shape function (Fig. 1(a)),

$$s(z) = \frac{1}{2} \text{erfc} \left(\frac{z_0 - z}{\sigma \sqrt{2}} \right), \quad (5)$$

which modulates the environment dielectric constant (Fig. 1(b)) as $\epsilon(z) = 1 + (\epsilon_b - 1)s(z)$, where ϵ_b is the bulk dielectric constant of the substrate. Note that the appropriate value of the bulk dielectric constant is the optical

dielectric constant (ϵ_∞) if the substrate atoms are not allowed to relax, and the low-frequency value if atomic relaxations are allowed. Here, we used the optical value for all cases, because we do not relax substrate atomic geometry for each defect configuration for computational expediency. In the example of MoS₂ on SiO₂ shown in Fig. 1, the MoS₂ monolayer is centered at $z = 0$, the substrate dielectric function smoothly ‘turns on’ centered at $z = z_0$ over a width controlled by σ , to the bulk value of $\epsilon_b = 2.65$ deep within the substrate. (The resulting thicknesses of the vacuum and dielectric slab regions are $L_z/2 + z_0$ and $L_z/2 - z_0$ respectively, where L_z is the length of the calculation cell normal to the 2D material, as shown in the figure S1 of the Supplemental Material.) Self-consistent solution of the modified Poisson equation with this dielectric profile replaces the Hartree term in the DFT calculation,³² and produces the bound charge at the surface of the continuum substrate shown in Fig. 1(c).

This substrate continuum model involves as-yet undetermined parameters σ and z_0 which both affect the proximity of the substrate dielectric response to the 2D material. We then constrain the continuum model parameters to reproduce the response of an explicit DFT substrate to charge distributions in the 2D material. First, we calculate the interaction energy of the Gaussian test charge with the DFT substrate,

$$E_{\text{int}}^{\text{DFT}} = E_{s+g} - E_s - E_g, \quad (6)$$

where E_{s+g} and E_s are DFT energies of the substrate alone, with and without an external Gaussian test charge placed at $z = 0$ (the center of the 2D material), and E_g is the electrostatic self energy of the Gaussian charge alone. Note that we use the model-charge-based correction scheme to handle the net charge in the supercell calculation of E_{s+g} , exactly as for the charged defects.¹⁷ Next, for a given dielectric profile based on the cavity shape function $s(z)$, we can directly calculate the interaction energy $E_{\text{int}}^{s(z)}$ of the test charge with the continuum dielectric by solving the modified Poisson equation in cylindrical coordinates, which we do using a Bessel function expansion as described in detail in Ref. 17. Finally, we select the cavity parameters such that $E_{\text{int}}^{s(z)} = E_{\text{int}}^{\text{DFT}}$. However, we have two parameters σ and z_0 , so we fix σ and determine z_0 to satisfy the above condition. (The resulting values of z_0 are listed in Table S1 of the Supplemental Material.) Fortunately, we find that the predictions for charged defects are independent of σ once it is smaller than ~ 0.3 Å, as detailed below in the discussion of Fig. 2. In summary, we use two DFT calculations of the substrate alone to determine the continuum model parameters, which can then be used for systematically studying the impact of that substrate on several charged defect configurations in 2D materials.

Beyond the electrostatic interaction of the defect captured by the substrate continuum model, the substrate modifies the electronic band structure of the 2D material itself, which is vital to capture because the defect ionization energies given by (3) and (4) depend on the CBM and VBM energies respectively. Fig. 1(d) summarizes

our approach to capture this effect. First, the continuum model accounts for the overall electrostatic potential shift at the location of the 2D material due to the substrate, which shifts the CBM and VBM equally, but does not change the band gap. Next, by aligning core levels (which are sensitive only to electrostatic potential) in density-of-states calculations of the substrate and substrate + perfect 2D material, we can identify the shifts of the VBM and CBM that are *beyond* electrostatic potential effects. Putting these together, we get the VBM and CBM shifts in the 2D material due to both the overall electrostatic potential and electronic effects beyond it. In the specific example of MoS₂/SiO₂ shown in Fig. 1(d), we find the offsets to be $\Delta\epsilon_{\text{VBM}} = +0.056$ eV and $\Delta\epsilon_{\text{CBM}} = -0.008$ eV for a net band gap reduction of 0.064 eV due to the SiO₂ substrate. We illustrate this process in greater detail below for hBN on SiO₂ and diamond, including with projected band structures to isolate the 2D material band structure on a substrate. Once again, our overall calculation procedure using the continuum methodology proposed here involves only two calculations of the substrate alone and one of the substrate with a perfect 2D material. Importantly, these calculations are required only once for the 2D material and substrate combination, and no explicit substrates are included in the large supercell calculations *per defect configuration*.

C. Computational details

We implemented the above technique and performed all calculations below in the open-source plane-wave DFT software, JDFTx.³⁷ We used the Garrity-Bennett-Rabe-Vanderbilt ultrasoft pseudopotentials at their recommended kinetic energy cutoffs of 20 and 100 Hartrees for the electronic wave function and charge density respectively.³⁸ All supercell calculations below additionally employ Brillouin zone sampling with a 2×2 Monkhorst-Pack k -mesh, and truncated Coulomb interactions to eliminate interactions with periodic images along the slab normal ‘ z ’ direction.³⁹

We use a 6×6 supercell with 30 Å and 16 Å lengths in the z direction for MoS₂ and hBN respectively, which is sufficient to completely converge results with the truncated Coulomb interactions. (For example, the ionization energy of the C_B defect in hBN/SiO₂ changes only by 20 meV when this length is increased from 16 Å to 30 Å.) We employ the local-density exchange-correlation functional for the MoS₂ systems in order to benchmark against previous explicit calculations,⁴⁰ and the Perdew-Burke-Ernzerhof generalized gradient functional⁴¹ with DFT-D2 dispersion correction⁴² for the hBN systems.

While the technique developed here applies readily to any DFT functional or many-body method, we employed semi-local exchange-correlation functionals to rapidly explore several systems for developing and testing our new method, including with large calculations of explicit substrates. Hybrid DFT and many-body perturbation theory, which typically predict the band edge positions and the gap with greater accuracy,^{43,44} may update the ab-

solute values of ionization energies. In particular, many-body perturbation theory techniques capture more substantial changes in the band edge positions and gap due to substrate screening that is not captured in DFT,⁸ which then impacts the ionization energies referenced to the band edges. However, semi-local DFT predicts the correct trends in the defect transition levels, as shown previously for free-standing hBN,^{18,23} and we restrict our focus to the DFT level for this initial test of the continuum methods.

For optimal lattice matching, the explicit-substrate MoS₂/SiO₂ and hBN/SiO₂ calculations respectively used 4×4 and 3×3 supercells of α -SiO₂(0001) slabs with six Si atomic layers, while the hBN/Diamond calculations used a 6×6 supercell of diamond(111) with eight C atomic layers. In each case, the lateral lattice constants were set to the optimal values for the 2D material, resulting in a 5.16%, 0.04% and 0.50% substrate strain in the MoS₂/SiO₂, hBN/SiO₂ and hBN/Diamond cases respectively. All dangling bonds on the substrate surfaces were passivated with H atoms. The atomic geometry of the substrate is optimized initially, and then held fixed for the defect supercell calculations for computational efficiency, while the atoms within the 2D material are fully relaxed in all calculations. (Note that this is a convenient benchmark for the continuum model calculations with the substrate dielectric constant set to ϵ_∞ , as discussed above. The continuum model can be used to predict results corresponding to full relaxation by replacing ϵ_∞ with the low-frequency dielectric constant at no additional computational cost.)

III. RESULTS AND DISCUSSION

A. Defects in MoS₂ on SiO₂

We start by testing our technique on the only charged defects in 2D materials for which previous calculations have explicitly included substrate effects: Re_{Mo} and Nb_{Mo} in MoS₂/SiO₂. Re and Nb have one more and less electron relative to Mo, so that these substitution defects act as a donor and an acceptor respectively. Fig. 2(a) shows the prediction of the charge transition level of these defects using the continuum methodology above. Both defects exhibit a reduction of the defect ionization energy by around 0.10-0.15 eV due to the SiO₂ substrate, which is a significant effect for defects that have initial ionization energies of 0.4-0.5 eV. (See Table S2 in the Supplemental Material for a listing of calculated ionization energies.) These continuum model results (in terms of ionization energy reduction) are in excellent agreement of within 0.05 eV with previous results from much more expensive explicit substrate calculations,⁴⁰ demonstrating the reliability of our method. Note that here and below, we present charge transition levels and defect ionization energies instead of the closely related charged defect formation energies because these are easier to standardize and compare across defects; the latter also depend on reference chemical potentials for each atom removed or

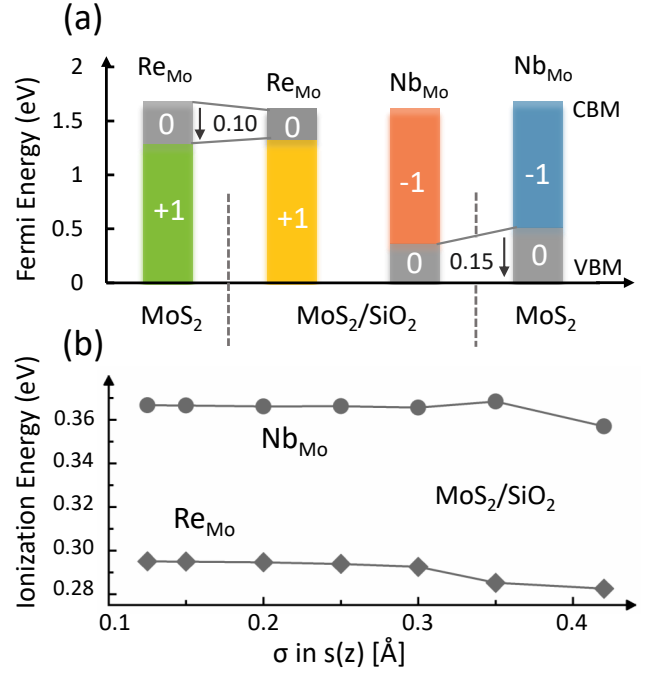


FIG. 2. Defect calculation in MoS₂ system. (a) The stable charge state of Re_{Mo} and Nb_{Mo} in MoS₂ and MoS₂/SiO₂ for Fermi energy ranging from VBM to CBM. The Fermi energy at the intersection of two different charge states ($q = +1$ and $q = 0$ for donor, $q = 0$ and $q = -1$ for acceptor) dictates the defect transition level. The corresponding defect ionization energies are denoted by the gray shadows. (b) The ionization energies of Re_{Mo} and Nb_{Mo} in MoS₂/SiO₂ as a function of σ .

added by the defect.

Fig. 2(b) shows the variation of the results with the one free parameter σ that sets the smoothness of the transition from vacuum to substrate dielectric constant. (As discussed above, z_0 , which sets the center of the transition of $s(z)$, is constrained using the response of a DFT substrate to a Gaussian test charge, for a given σ .) The results are insensitive to σ as long as it is small enough, with variations in the predicted ionization energies far below 0.01 eV for $\sigma < 0.3$ Å. We recommend $\sigma = 0.2$ Å for subsequent calculations, which is small enough to avoid overlap of 2D material charge density with the substrate dielectric response, and yet large enough to exhibit a smooth dielectric constant variation that is easily resolvable on a charge density grid with resolution ~ 0.1 Å (kinetic energy cutoff ~ 100 Hartrees).

Intuitively, the substrate dielectric screening stabilizes charged states of defects, making them easier to ionize and thereby shifting the charge transition levels closer to the corresponding band edges (VBM for acceptor and CBM for donors). The strong decrease of defect ionization energies in semiconductor MoS₂ is desirable for dopants for 2D electronics, as it makes it possible to introduce charge carriers to the bands at lower temperatures. Yet, the same effect can be undesirable for defect levels sought after for quantum information, where dis-

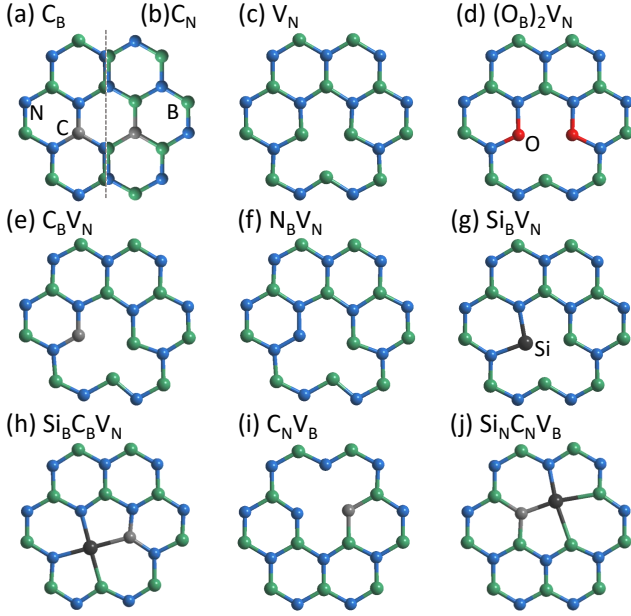


FIG. 3. Optimized atomic configurations of promising hBN defects considered here using the standard notation that C_B denotes C substituting a B atom, V_N denotes a vacancy of N, and compound defects such as C_BV_N indicates that such substitutions / vacancies occur on adjacent atoms.

tance from band edges enhances life time of defect excited states, as we discuss next for hBN.

B. Defects in hBN on SiO_2 and diamond

Defects in hBN are the subject of increasing recent interest as candidates for single-photon emission in a 2D analogue of the long-studied nitrogen-vacancy center in diamond. While several recent studies have characterized the properties of spin and charge states in hBN,^{10,11,18,23,45,46} none so far account for the effect of the substrate. We therefore take advantage of the method established above to systematically and rapidly investigate substrate effects on several promising hBN defects, with atomic configurations shown in Fig. 3.

First, we determine the band position changes of hBN, when placed on $\text{SiO}_2(0001)$ and diamond(111) substrates, which is required for ionization energy calculations using (3) and (4). For hBN/ SiO_2 , we do this by calculating the density of states (DOS) and unfolding the band structure of the 6×6 hBN/ 3×3 SiO_2 supercell to the Brillouin zone of hBN unit cell.⁴⁷ The unfolding clearly picks out the hBN bands that are commensurate with the unit cell, as shown by the red lines in Fig. 4. The resulting band gap is 4.64 eV, 0.04 eV smaller than in free-standing hBN. On the other hand, hBN and diamond unit cells are already lattice matched within 0.5%, requiring no supercell calculations for determining band alignments. We therefore do not require band structure unfolding in this case, and instead use orbital projections to weight the band structure and identify hBN contributions as shown in Fig. 5.

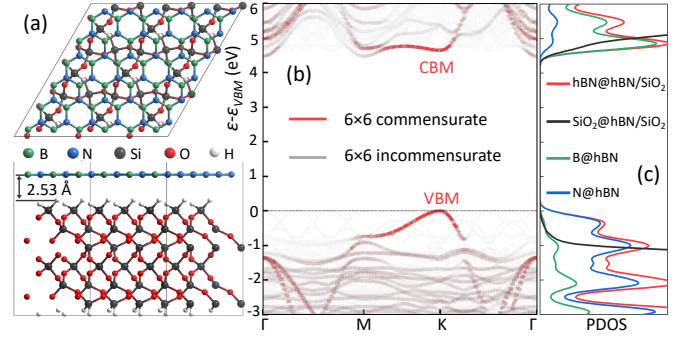


FIG. 4. (a) Atomic configuration of (defect-free) 6×6 hBN/ 3×3 SiO_2 in top and side views. (b) Band structure unfolded to Brillouin zone of hBN unit cell, with red and gray colors respectively indicating components commensurate and incommensurate with the hBN unit cell, and (c) corresponding DOS.

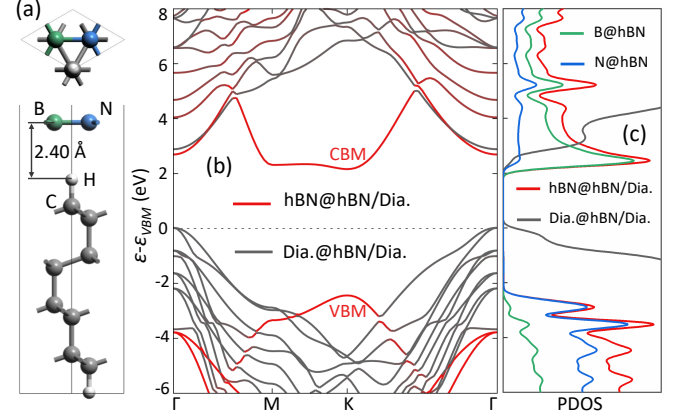


FIG. 5. (a) Atomic configuration of hBN/diamond in top and side views. (b) Projected band structure with red and black colors indicating weights of hBN and diamond atomic orbital projections respectively, and (c) corresponding DOS.

Stronger dielectric screening in diamond reduces the band gap further to 4.60 eV, as shown in Fig. 5(b).

Next, after identifying the band gap modifications, we also need to determine the band edge offsets, ε_{VBM} and ε_{CBM} . As discussed above, these offsets consist of an overall electrostatic potential shift due to the substrate that is captured by the solvation model, specifically shifting both VBM and CBM up by 0.94 eV in hBN/ SiO_2 and by 1.00 eV in hBN/Diamond relative to free-standing hBN (dashed lines in Fig. 6). Further, by aligning the core levels in the DOS of isolated hBN and hBN with substrates, we can identify the shifts in the VBM and CBM beyond the overall electrostatic potential shift. The band edge offset is not determined from the continuum model and requires explicit DOS calibration. This yields a $\Delta\varepsilon_{\text{VBM}} = -0.006$ eV and $\Delta\varepsilon_{\text{CBM}} = -0.042$ eV for hBN/ SiO_2 , and $\Delta\varepsilon_{\text{VBM}} = -0.02$ eV and $\Delta\varepsilon_{\text{CBM}} = -0.10$ eV for hBN/Diamond. Adding these offsets yields the final reference band edges for ionization energy calculations within the continuum model (solid lines in Fig. 6).

The total energy calculations using the continuum

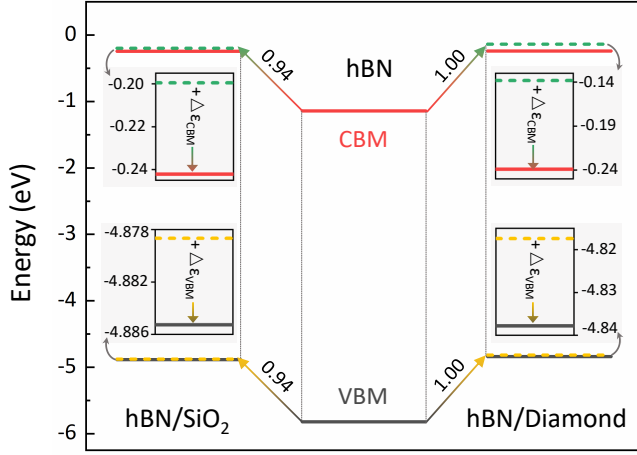


FIG. 6. Determination of VBM and CBM of hBN on substrates. From hBN to hBN/SiO₂, VBM and CBM both shift up by 0.94 eV due to the substrate electrostatic potential, and then shift $\Delta\epsilon_{\text{VBM}} = -0.006$ eV and $\Delta\epsilon_{\text{CBM}} = -0.042$ eV as determined from DOS calculations aligned by core levels (shown magnified in the insets). Similarly, diamond introduces an electrostatic shift of 1.00 eV, followed by $\Delta\epsilon_{\text{VBM}} = -0.02$ eV and $\Delta\epsilon_{\text{CBM}} = -0.10$ eV.

model along with the band edge positions determined above are now all we need to determine the defect ionization energies, which are the charge transition levels relative to the appropriate band edge. Fig. 7(a) displays the calculated donor ionization energies for several defects in hBN, hBN/SiO₂ and hBN/Diamond, while Fig. 7(b) shows acceptor ionization energies for several defects, all of whose geometries are shown in Fig. 3. Note that many defects are shown in both panels because they can act as both donors and acceptors. The defects are all deep in hBN with ionization energies in the range of 2.14–4.01 eV. Compared to free-standing hBN, ionization energies decrease by 0.27–0.33 eV in hBN/SiO₂, and 0.47–0.64 eV in hBN/Diamond due to increased dielectric screening by the substrate. However, even with this systematic reduction in ionization energies, all these defect levels remain deep – much larger than thermal and phonon energies in the material – indicating that they are viable to exhibit a long coherence time even after substrate modifications to their energetics.

To confirm the accuracy of these results, we also carried out explicit 2D material + substrate calculations for a few test cases. Specifically, we performed explicit calculations for the C_B, V_N and N_BV_N donor ionization energies in hBN/SiO₂, and the donor ionization energies of C_B and V_N as well as the acceptor ionization energy of V_N in hBN/Diamond. We find that our continuum model predictions are accurate to within 0.10 – 0.12 eV for the hBN/SiO₂ cases, and to within 0.11 – 0.16 eV for hBN/diamond (see Table S3 in the Supplemental Material for individual values). While the absolute errors are greater than in the MoS₂ case, note that the overall magnitudes of the substrate effects are larger for hBN, resulting in a similar relative accuracy. Similarly,

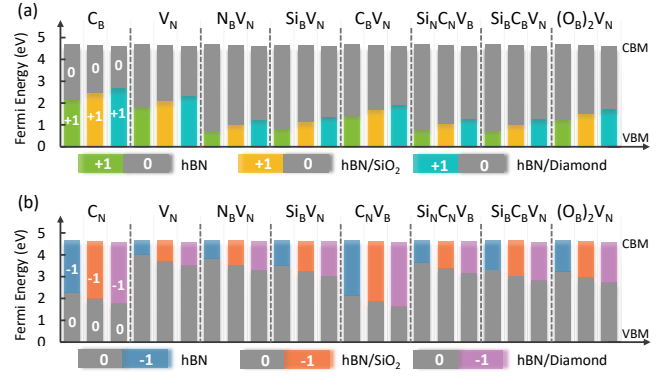


FIG. 7. The stable charge state of all hBN defects shown in Fig. 3 as a function of Fermi energy ranging from VBM to CBM. Fermi energy at the intersection of two different charge states, (a) $q = +1$ and $q = 0$ for donor, and (b) $q = 0$ and $q = -1$ for acceptor, dictates the defect transition levels. The corresponding defect ionization energies are denoted by gray shadows.

TABLE I. Comparison of ionization energy reduction due to substrate predicted by self-consistent continuum model calculations for all above defects, with a single non-self-consistent estimate for each 2D material - substrate combination using Eq. 7 with the same continuum model. (See Table S5 in Supplemental Material for individual results for each defect.)

Donors	Self-consistent	Eq. 7
$\Delta IE_{\text{MoS}_2/\text{SiO}_2}$ (eV)	0.10	0.10
$\Delta IE_{\text{hBN/SiO}_2}$ (eV)	0.31 – 0.33	0.32
$\Delta IE_{\text{hBN/Diamond}}$ (eV)	0.58 – 0.62	0.60
Acceptors	Continuum Model	Eq. 7
$\Delta IE_{\text{MoS}_2/\text{SiO}_2}$ (eV)	0.15	0.14
$\Delta IE_{\text{hBN/SiO}_2}$ (eV)	0.27 – 0.29	0.27
$\Delta IE_{\text{hBN/Diamond}}$ (eV)	0.47 – 0.52	0.48

formation energies of neutral defects in hBN/SiO₂ and hBN/Diamond from the continuum model are accurate to within 0.03–0.16 eV of the explicit substrate calculations (see Table S4 in the Supplemental Material), with the difference arising mainly from effects beyond the dielectric response such as Pauli repulsion from substrate electrons. Overall, this accuracy is remarkable considering that the continuum model calculations required at most 72 atoms compared to 252 and 432 atoms for hBN/SiO₂ and hBN/Diamond (in addition to just 30 bohrs vacuum size compared to 56.7 and 47.2 bohrs respectively). This amounts to a 40–200× reduction in computational effort, making it now possible to rapidly explore defect energetics with realistic treatment of substrate effects.

C. Ionization energy reduction estimates

We have so far presented predictions of the ionization energy of several donor and acceptor defects in three 2D material/substrate combinations, and compared against

explicit substrate calculations to establish the accuracy of our technique. Table I summarizes the *reduction* in ionization energy ΔIE from the free-standing 2D material to the 2D material on the substrate in each of these combinations. Note that the reduction in ionization energy is almost the same across all defects within each material/substrate combination.

The reason for this equivalence in ionization energy reduction is that most charged defects have a fairly-localized charge distribution which does not change appreciably upon the introduction of a substrate. The charged defect corrections schemes already take advantage of this fact to remove the periodic interaction between defects by computing the self-energy of a Gaussian model charge in periodic and isolated boundary conditions.^{15,17} We could then similarly estimate the reduction in ionization energy of charged defects as the electrostatic stabilization of a Gaussian model charge,

$$\Delta IE \approx E_g^{\text{iso}}(2D) - E_g^{\text{iso}}(2D/\text{sub}) + \begin{cases} -\Delta\epsilon_{\text{CBM}}, & \text{Donors} \\ +\Delta\epsilon_{\text{VBM}}, & \text{Acceptors} \end{cases} \quad (7)$$

where $E_g^{\text{iso}}(2D)$ and $E_g^{\text{iso}}(2D/\text{sub})$ are the self energies of the Gaussian model charge in isolated boundary conditions in the dielectric model of the 2D material alone and of the 2D material on the substrate. (These quantities are already used in the charge defect correction for the free-standing 2D material and 2D material on continuum model substrate respectively.) The second term in Eq. 7 accounts for the change in ionization energy due to the substrate-induced shift of the corresponding band edge position, which serves as the reference for defining ionization energies (Eqs. 3 and 4). Note that all quantities in Eq. 7 depend on the 2D material and substrate combination alone, and not on a specific defect.

The final column of Table. I shows the results of applying Eq. 7 to each of the three 2D material/substrate combinations studied above. We find that this simple estimate agrees with a typical accuracy of 0.02 eV with the continuum model predictions and a maximum deviation of about 0.04 eV. (See Table S5 in Supplemental Material additionally shows individual results for each defect, compared with this estimate.) This now makes it possible to rapidly estimate the ionization energy of *any* defect without even performing self-consistent DFT + contin-

uum model calculations of each defect separately. We only need to calculate the ionization energy of all defects of interest in a free-standing 2D material, construct the continuum model for a substrate of interest as described above, and compute a single number using Eq. 7 to shift all free-standing defect ionization energies to the corresponding values on substrates.

IV. CONCLUSIONS

We have demonstrated a general framework to efficiently and accurately calculate energies and related properties of charged defects in 2D materials on substrates. We resolve the challenge of first-principles evaluation of such systems by treating the substrate as a continuous medium, with its electrostatic response replaced by a continuum dielectric function. Results obtained by this method agree very well with explicit calculations that directly include substrate atoms, but at a small fraction of the computational effort.

This methodology applies to arbitrary combinations of defects, 2D materials and substrates, potentially enabling high-throughput screening of not only defects with unique properties, but also material-substrate combinations targeting desired defect properties. As an example, application of this method to defects in MoS₂ and hBN on SiO₂ and diamond substrates reveals that enhanced screening from surrounding environments can significantly change transition levels. This provides an invaluable input for the experimental identification of 2D defects for quantum information applications such as single photon emission, fully accounting for monolayer 2D materials on realistic substrates, as well as in multilayer 2D materials and 2D heterostructures in future work.

ACKNOWLEDGMENTS

We acknowledge startup funding from the Department of Materials Science and Engineering at Rensselaer Polytechnic Institute. All calculations were carried out at the Center for Computational Innovations at Rensselaer Polytechnic Institute.

* sundar@rpi.edu

¹ M. Toth and I. Aharonovich, Ann. Rev. Phys. Chem. **70**, 123 (2019).

² Z. Lin, B. R. Carvalho, E. Kahn, R. Lv, R. Rao, H. Terrones, M. A. Pimenta, and M. Terrones, 2D Mater. **3**, 022002 (2016).

³ D. Wang, X.-B. Li, D. Han, W. Q. Tian, and H.-B. Sun, Nano Today **16**, 30 (2017).

⁴ H. I. Rasool, C. Ophus, and A. Zettl, Adv. Mater. **27**, 5771 (2015).

⁵ J. Hong, C. Jin, J. Yuan, and Z. Zhang, Adv. Mater. **29**, 1606434 (2017).

⁶ A. Alkauskas, M. D. McCluskey, and C. G. Van de Walle, J. Appl. Phys. **119**, 181101 (2016).

⁷ S. Zhang, J. Phys.: Cond. Matt. **14**, R881 (2002).

⁸ M. H. Naik and M. Jain, Phys. Rev. Mater. **2**, 084002 (2018).

⁹ A. Singh, A. Manjanath, and A. K. Singh, J. Phys. Chem. C **122**, 24475 (2018).

¹⁰ S. A. Tawfik, S. Ali, M. Fronzi, M. Kianinia, T. T. Tran, C. Stampfl, I. Aharonovich, M. Toth, and M. J. Ford, Nanoscale **9**, 13575 (2017).

¹¹ A. Sajid, J. R. Reimers, and M. J. Ford, Phys. Rev. B **97**, 064101 (2018).

- ¹² S. Gupta, J.-H. Yang, and B. I. Yakobson, *Nano Lett.* **19**, 408 (2019).
- ¹³ G. Grosso, H. Moon, B. Lienhard, S. Ali, D. K. Efetov, M. M. Furchi, P. Jarillo-Herrero, M. J. Ford, I. Aharonovich, and D. Englund, *Nature Commun.* **8**, 705 (2017).
- ¹⁴ T. T. Tran, C. Elbadawi, D. Totonjian, C. J. Lobo, G. Grosso, H. Moon, D. R. Englund, M. J. Ford, I. Aharonovich, and M. Toth, *ACS Nano* **10**, 7331 (2016).
- ¹⁵ H.-P. Komsa and A. Pasquarello, *Phys. Rev. Lett.* **110**, 095505 (2013).
- ¹⁶ D. Wang, D. Han, X.-B. Li, S.-Y. Xie, N.-K. Chen, W. Q. Tian, D. West, H.-B. Sun, and S. Zhang, *Phys. Rev. Lett.* **114**, 196801 (2015).
- ¹⁷ R. Sundararaman and Y. Ping, *J. Chem. Phys.* **146**, 104109 (2017).
- ¹⁸ F. Wu, A. Galatas, R. Sundararaman, D. Rocca, and Y. Ping, *Phys. Rev. Mater.* **1**, 071001 (2017).
- ¹⁹ D. Wang, D. Han, X.-B. Li, N.-K. Chen, D. West, V. Meunier, S. Zhang, and H.-B. Sun, *Phys. Rev. B* **96**, 155424 (2017).
- ²⁰ C. Freysoldt and J. Neugebauer, *Phys. Rev. B* **97**, 205425 (2018).
- ²¹ D. Wang, X.-B. Li, and H.-B. Sun, *Nanoscale* **9**, 11619 (2017).
- ²² M. H. Naik and M. Jain, *Comput. Phys. Comm.* **226**, 114 (2018).
- ²³ T. J. Smart, F. Wu, M. Govoni, and Y. Ping, *Phys. Rev. Mater.* **2**, 124002 (2018).
- ²⁴ D. Wang, D. Han, D. West, N.-K. Chen, S.-Y. Xie, W. Q. Tian, V. Meunier, S. Zhang, and X.-B. Li, *npj Comput. Mater.* **5**, 8 (2019).
- ²⁵ J. Tomasi, B. Mennucci, and R. Cammi, *Chem. Rev.* **105**, 2999 (2005).
- ²⁶ A. V. Marenich, C. J. Cramer, and D. G. Truhlar, *J. Phys. Chem. B* **113**, 6378 (2009).
- ²⁷ O. Andreussi, I. Dabo, and N. Marzari, *J. Chem. Phys.* **136**, 064102 (2012).
- ²⁸ H. Xiao, T. Cheng, W. A. Goddard III, and R. Sundararaman, *J. Am. Chem. Soc.* **138**, 483 (2016).
- ²⁹ A. T. B. Jason D. Goodpaster and M. Head-Gordon, *J. Phys. Chem. Lett.* **7**, 1471 (2016).
- ³⁰ R. Sundararaman, K. Letchworth-Weaver, and K. A. Schwarz, *J. Chem. Phys.* **148**, 144105 (2018).
- ³¹ R. Sundararaman, D. Gunceler, and T. A. Arias, *J. Chem. Phys.* **141**, 134105 (2014).
- ³² D. Gunceler, K. Letchworth-Weaver, R. Sundararaman, K. A. Schwarz, and T. A. Arias, *Model. Simul. Mater. Sci. Eng.* **21**, 074005 (2013).
- ³³ R. Sundararaman, K. A. Schwarz, K. Letchworth-Weaver, and T. A. Arias, *J. Chem. Phys.* **142**, 054102 (2015).
- ³⁴ R. Sundararaman and W. A. Goddard, *J. Chem. Phys.* **142**, 064107 (2015).
- ³⁵ S. Zhang and J. Northrup, *Phys. Rev. Lett.* **67**, 2339 (1991).
- ³⁶ D. Han, Y. Y. Sun, J. Bang, Y. Y. Zhang, H.-B. Sun, X.-B. Li, and S. B. Zhang, *Phys. Rev. B* **87**, 155206 (2013).
- ³⁷ R. Sundararaman, K. Letchworth-Weaver, K. A. Schwarz, D. Gunceler, Y. Ozhakes, and T. Arias, *SoftwareX* **6**, 278 (2017).
- ³⁸ K. F. Garrity, J. W. Bennett, K. M. Rabe, and D. Vanderbilt, *Comput. Mater. Sci.* **81**, 446 (2014).
- ³⁹ R. Sundararaman and T. Arias, *Phys. Rev. B* **87**, 165122 (2013).
- ⁴⁰ J.-Y. Noh, H. Kim, M. Park, and Y.-S. Kim, *Phys. Rev. B* **92**, 115431 (2015).
- ⁴¹ J. P. Perdew, K. Burke, and M. Ernzerhof, *Phys. Rev. Lett.* **77**, 3865 (1996).
- ⁴² S. Grimme, *J. Comput. Chem.* **27**, 1787 (2006).
- ⁴³ C. Freysoldt, P. Rinke, and M. Scheffler, *Phys. Rev. Lett.* **103**, 056803 (2009).
- ⁴⁴ F. Hüsler, T. Olsen, and K. S. Thygesen, *Phys. Rev. B* **87**, 235132 (2013).
- ⁴⁵ M. Abdi, J.-P. Chou, A. Gali, and M. B. Plenio, *ACS Photonics* **5**, 1967 (2018).
- ⁴⁶ J. R. Reimers, A. Sajid, R. Kobayashi, and M. J. Ford, *J. Chem. Theory Comput.* **14**, 1602 (2018).
- ⁴⁷ V. Popescu and A. Zunger, *Phys. Rev. B* **85**, 085201 (2012).